# Active Damping of Power Control for Grid-Forming Inverters in LC Resonant Grids

Liu, Shiyi; Wu, Heng; Wang, Xiongfei; Bosma, Theo; van der Burgt , Jos; Sauba, Ganesh; Singh, Ravi

*Published in:*
2022 IEEE Energy Conversion Congress and Exposition, ECCE 2022

*DOI (link to publication from Publisher):*
10.1109/ECCE50734.2022.9948116



*Publication date:*
2022

*Document Version*
Accepted author manuscript, peer reviewed version

# Active Damping of Power Control for Grid-Forming Inverters in LC Resonant Grids

Shiyi Liu*†, Heng Wu*, Xiongfei Wang*, Theo Bosma†, Jos van der Burgt†, Ganesh Sauba†, Ravi Singh†

*Department of Energy Technology
Aalborg University
Aalborg, Denmark
{shli, hew, xwa}@energy.aau.dk

†Energy System Group
DNV
Arnhem, Netherland
{Shiyi.Liu, Theo.Bosma, Jos.vanderBurgt, Ganesh.Sauba, Ravi.Singh}@DNV.com

***Abstract*—This paper derives the small-signal model of grid-forming (GFM) inverters considering the presence of shunt capacitor in the power grid. It is pointed out that the shunt capacitor introduces two additional resonant peaks in the loop gain of power control loops, in addition to the fundamental-frequency resonant peak that is identified in the prior art. Based on the findings, the active damping control is modified to dampen all three resonant peaks to guarantee the stable operation of GFM inverters. Finally, simulation and experimental tests are carried out to corroborate the theoretical analysis.**

***Index Terms*—Grid-forming, small-signal model, stability, power control, active damping, voltage-source inverters.**

## I. Introduction

Nowadays, the grid-forming (GFM) control emerges as a suitable solution for operating inverters under the weak grid condition. Being controlled as a voltage source rather than a current source, the GFM inverter can operate stably even if the short circuit ratio (SCR) of the power grid approaches 0 [1].

The GFM inverter synchronizes with the power grid by regulating its active power while maintaining its terminal voltage by regulating its reactive power [2]. Hence, the design of active and reactive power control loops is crucial for the stable operation of GFM inverters [2]. By considering GFM inverters with a single L filter that is connected with inductive grid impedance, it is revealed in [3], [4] that there is a resonant peak at the grid fundamental frequency in the loop gain of the power control loop, which can lead to the unstable operation of GFM inverters [5]. To dampen this resonant peak, the active damping method based on the virtual resistor is reported in [3]. In [6] the parameters tuning guideline of the virtual resistor as well as its associated high-pass filter are elaborated.

In [4], it is pointed out that multiple resonant peaks, rather than a single fundamental-frequency resonant peak, appear in the power control loop of GFM inverters when there are shunt capacitors at the point of common coupling (PCC) of ac grids. However, their impact on system stability and the appropriate active damping control are not considered therein [4], [7], which might be acceptable in some scenarios where the shunt capacitor is small and has limited impact on the low-frequency dynamics of power control loops [3]. Yet for scenarios with large shunt ac capacitors (e.g. contributed by capacitive loads or shunt capacitor branch used for reactive power compensation), neglecting the impact of capacitors in designing the active damping control may fail to stabilize the GFM inverter, as will be demonstrated in this paper.

To reveal the dynamic impact of shunt ac capacitors on the stability of GFM inverters and the design of active damping control, this paper derives the small-signal model of GFM inverters with shunt ac capacitors. Based on the developed model, it is shown that two additional resonant peaks emerge in power control loops of GFM inverters, due to the presence of shunt ac capacitors. By investigating the characteristic of these two extra resonant peaks, the impact of shunt ac capacitors can be analytically derived and the guideline for designing active damping control is also given. Finally, simulation and experimental tests are carried out to corroborate the theoretical analysis.

## II. Small-signal modelling method

### A. System description

Fig. 1 shows the single-line diagram of a three-phase GFM inverter. The active damping method is adopted in this work to damp out the resonant peak [3]. The GFM inverter is connected to the PCC through a LC filter, where $Z_g$ is the grid impedance. $C_g$ represents the shunt ac capacitor, and its stability impact is the focus of this work. $V_{dc}$ denotes the constant DC voltage, which is either an energy storage unit or a front-end converter connected to the DC-link [3]. $P_0$, $Q_0$, $v_{inv}$ and $v_g$ denote the output active power, reactive power,

The work is supported by the European Union's Horizon 2020 Research and Innovation Program through the Marie Sklodowska-Curie under Grant 861398.

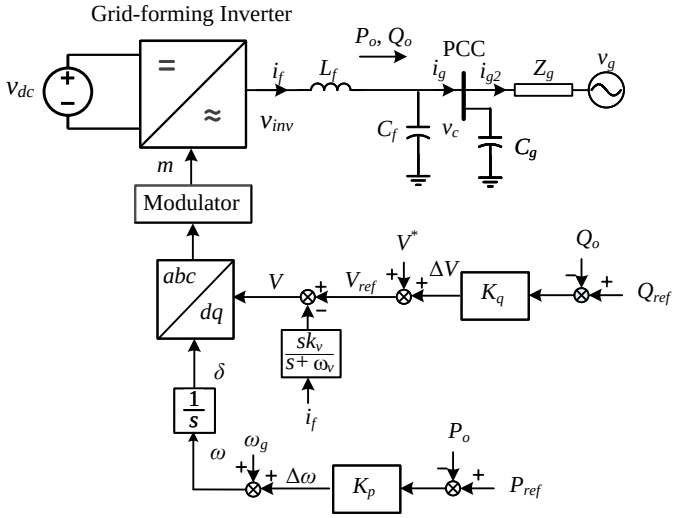


**Fig. 1:** Grid-forming voltage-source inverter.

the inverter bridge voltage and grid voltage respectively. $v_c$ represents the voltage of the PCC while $i_f$ is the current of filter inductance $L_f$, $i_g$ and $i_{g2}$ represent the current of the PCC and the grid.

The GFM inverter is synchronized with the power grid through the active power control, where the commonly used power synchronization control is adopted in this work, which can be expressed as [8].

$$\delta = \frac{1}{s}[\omega_g + K_p(P_{ref} - P_0)] \tag{1}$$

where $P_{ref}$ denotes the reference of active power and $\delta$ is the reference of angle. $\omega_g$ denotes the grid angular frequency while $K_p$ represents the active power-frequency droop coefficient.

The reactive power is controlled by adjusting the voltage magnitude, which is given by

$$V = V^* + K_q(Q_{ref} - Q_0) - i_f\frac{sk_v}{s+\omega_v} \tag{2}$$

where $Q_{ref}$ and $V$ denote the reference of reactive power and voltage magnitude while $V^*$ denotes the nominal voltage magnitude. $K_q$ represents the reactive power-voltage droop coefficient. $\frac{sk_v}{s+\omega_v}$ is the active damping with a high-pass filter ($\omega_v$ represents the cut-off frequency of the high-pass filter), which is further added to damp out the resonant peak of power control loops of GFM inverters [3].

### *B. Small-signal modeling*

It is noted that the control is implemented in the dq frame where the $d$-axis and $q$-axis components are controlled separately. Without loss of generality, the output variables are defined as $y_{dq} = \begin{bmatrix} y_d & y_q \end{bmatrix}^T$, whereas the input variables are defined as $x_{dq} = \begin{bmatrix} x_d & x_q \end{bmatrix}^T$. Their relationship can be generally expressed as

$$\begin{bmatrix} y_d \\ y_q \end{bmatrix} = \begin{bmatrix} G_{11}(s) & G_{12}(s) \\ G_{21}(s) & G_{22}(s) \end{bmatrix} \begin{bmatrix} x_d \\ x_q \end{bmatrix} \tag{3}$$

The instantaneous active power and reactive power can be calculated as shown in (4). It should be noted that the factor $\frac{3}{2}$ can be omitted if the modeling is performed based on per unit (p.u.) value.

$$\begin{cases} P &= \frac{3}{2}(i_{gd}v_{cd} + i_{gq}v_{cq}) \\ Q &= \frac{3}{2}(i_{gd}v_{cq} - i_{gq}v_{cd}) \end{cases} \tag{4}$$

For convenience, a matrix $J$ can be defined as

$$J = \begin{bmatrix} 0 & -1 \\ 1 & 0 \end{bmatrix} \tag{5}$$

Afterwards (4) can be rewritten as

$$\begin{bmatrix} P \\ Q \end{bmatrix} = \frac{3}{2}\begin{bmatrix} v_{cdq}^T i_{gdq} \\ v_{cdq}^T J i_{gdq} \end{bmatrix} \tag{6}$$

By following the same assumptions as proposed in [9], all state variables $x$ in Fig. 1 can be represented as $x = X_0 + \hat{x}$, where $X_0$ represents the corresponding steady-state value [10], and $\hat{x}$ is the small signal perturbation. Hence, the state variables can be represented by their stead-state values with small-signal perturbations, i.e.,

$$\begin{aligned} i_{dq} &= I_{dq0} + \hat{i}_{dq} \\ v_{dq} &= V_{dq0} + \hat{v}_{dq} \\ \begin{bmatrix} \delta \\ V \end{bmatrix} &= \begin{bmatrix} \delta_0 \\ V_0 \end{bmatrix} + \begin{bmatrix} \hat{\delta} \\ \hat{V} \end{bmatrix} \\ \begin{bmatrix} P \\ Q \end{bmatrix} &= \begin{bmatrix} P_0 \\ Q_0 \end{bmatrix} + \begin{bmatrix} \hat{P} \\ \hat{Q} \end{bmatrix} \\ sin(\delta_0 + \hat{\delta}) &\approx sin\delta_0 + cos\delta_0\hat{\delta} \\ cos(\delta_0 + \hat{\delta}) &\approx cos\delta_0 - sin\delta_0\hat{\delta} \end{aligned} \tag{7}$$

By substituting (7) into (6), the small-signal representation of the model active and reactive power output can be described in the following form

$$\begin{bmatrix} \hat{P} \\ \hat{Q} \end{bmatrix} = \frac{3}{2}\left(\begin{bmatrix} I_{gdq0}^T \\ -I_{gdq0}^T J \end{bmatrix}\hat{v}_{cdq} + \begin{bmatrix} V_{cdq0}^T \\ V_{cdq0}^T J \end{bmatrix}\hat{i}_{gdq}\right) \tag{8}$$

According to Fig. 1, the dynamics of the active damping control in controller dq frame can be expressed as

$$\begin{aligned} \hat{v}_{invdq}^c &= \hat{v}_{invdqref}^c - AD(s)\hat{i}_{fdq}^c \\ AD(s) &= \frac{sk_v}{s+\omega_v} \end{aligned} \tag{9}$$

where the superscript $c$ represents the controller dq frame. The relationship between the controller and system dq frame can be described as Fig. 2. Assuming $\delta_g$ is 0, then the phase angle difference between the controller and the system dq frame is equal to $\delta$.

Based on Fig. 1 and Fig. 2, after transforming $\hat{v}_{invdq}^c$ to system dq frame, (9) can be rewritten as

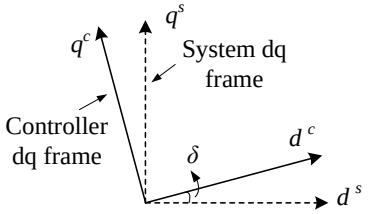


**Fig. 2:** Controller dq frame and system dq frame.

$$\begin{aligned}\hat{v}_{invdq} &= \begin{bmatrix} -V_{invq0} - AD(s)I_{fq0} & cos\delta_0 \\ V_{invd0} + AD(s)I_{fd0} & sin\delta_0 \end{bmatrix} \begin{bmatrix} \hat{\delta} \\ \hat{V} \end{bmatrix} \\ &- AD(s)\hat{i}_{fdq}\end{aligned} \tag{10}$$

Assuming $\hat{v}_{gdq} = 0$, it can be concluded from Fig. 1 that

$$\begin{aligned}\frac{d\hat{i}_{fdq}}{dt} &= \frac{\hat{v}_{invdq}}{L_f} - \frac{\hat{v}_{cdq}}{L_f} - \frac{R_f}{L_f}\hat{i}_{fdq} + \omega_g \begin{bmatrix} \hat{i}_{fq} \\ -\hat{i}_{fd} \end{bmatrix} \\ \frac{d\hat{v}_{cdq}}{dt} &= \frac{1}{(C_f + C_g)}(\hat{i}_{fdq} - \hat{i}_{g2dq}) + \omega_g \begin{bmatrix} \hat{v}_{cq} \\ -\hat{v}_{cd} \end{bmatrix} \\ \frac{d\hat{v}_{cdq}}{dt} &= \frac{1}{C_f}(\hat{i}_{fdq} - \hat{i}_{gdq}) + \omega_g \begin{bmatrix} \hat{v}_{cq} \\ -\hat{v}_{cd} \end{bmatrix} \\ \frac{d\hat{i}_{g2dq}}{dt} &= \frac{\hat{v}_{cdq} - R_g\hat{i}_{g2dq}}{L_g} + \omega_g \begin{bmatrix} \hat{i}_{g2q} \\ -\hat{i}_{g2d} \end{bmatrix}\end{aligned} \tag{11}$$

For obtaining accurate small-signal model of GFM inverter, introducing the Laplace transformation and substituting (10) into (12) [11], which leads to

$$\begin{aligned}&\begin{bmatrix} -V_{invq0} - AD(s)I_{fq0} & cos\delta_0 \\ V_{invd0} + AD(s)I_{fd0} & sin\delta_0 \end{bmatrix} \begin{bmatrix} \hat{\delta} \\ \hat{V} \end{bmatrix} - AD(s)\hat{i}_{fdq} \\ &\quad = \hat{v}_{cdq} + (sL_f + R_f + L_f\omega_g J)\hat{i}_{fdq} \\ &\hat{i}_{gdq} = \hat{i}_{g2dq} + (sC_g + C_g\omega_g J)\hat{v}_{cdq} \\ &\hat{i}_{fdq} = \hat{i}_{gdq} + (sC_f + C_f\omega_g J)\hat{v}_{cdq} \\ &\hat{v}_{cdq} = (sL_g + R_g + L_g\omega_g J)\hat{i}_{g2dq}\end{aligned} \tag{12}$$

Based on (12), the complete small signal model of a GFM inverter can be derived as shown in Fig. 3, where,

$$\begin{aligned}Z_f(s) &= sL_f + R_f + L_f\omega_g J \\ Y_g(s) &= sC_g + C_g\omega_g J \\ Y_f(s) &= sC_f + C_f\omega_g J \\ Z_g(s) &= sL_g + R_g + L_g\omega_g J\end{aligned} \tag{13}$$

According to Fig. 3, the transfer function from $\begin{bmatrix} \hat{\delta} & \hat{V} \end{bmatrix}^T$ to $\begin{bmatrix} \hat{P} & \hat{Q} \end{bmatrix}^T$ can be expressed as

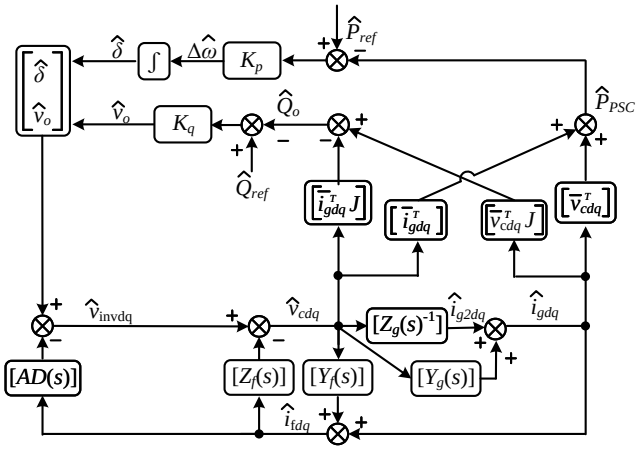


**Fig. 3:** Small Signal Model of a GFM inverter.

$$\begin{aligned}\begin{bmatrix} \hat{P} \\ \hat{Q} \end{bmatrix} &= [1 + Z_f(s)(Y_f(s) + Y_g(s))]^{-1} \\ &\bullet \{1 + AD(s)[(Y_f(s) + Y_g(s)) + Z_g(s)^{-1}] \\ &\bullet [1 + Z_f(s)(Y_f(s) + Y_g(s))]^{-1}\} \\ &\bullet \begin{bmatrix} -V_{invq0} - AD(s)I_{fq0} & cos\delta_0 \\ V_{invd0} + AD(s)I_{fd0} & sin\delta_0 \end{bmatrix} \begin{bmatrix} \hat{\delta} \\ \hat{V} \end{bmatrix} \\ &= G_{PQ}(s) \begin{bmatrix} \hat{\delta} \\ \hat{V} \end{bmatrix}\end{aligned} \tag{14}$$

To decouple the active/reactive power control loop shown in Fig. 3, $\hat{V}$ can be first set to be constant to calculate the transfer function for active power control loop. Afterwards, $\hat{\delta}$ can be set to zero to compute the transfer function of the reactive power control loop [3]. In the end, the open-loop transfer function of active and reactive power control loops of a GFM inverter can thus be derived as shown in (15), which is also displayed in Fig. 4.

$$\begin{aligned}T_P &= G_{\delta P}\frac{K_p}{s} \\ T_Q &= G_{VQ}K_q\end{aligned} \tag{15}$$

Where,

$$\begin{aligned}G_{PQ}(s)(1,1) &= G_{\delta P} \\ G_{PQ}(s)(2,2) &= G_{VQ}\end{aligned} \tag{16}$$

The poles of $T_P$ and $T_Q$ can be calculated by using (15), which is given by

$$\begin{cases} p_{1,2} &= \pm j\omega_g \\ p_{3,4} &= \pm j(\sqrt{\frac{L_f + L_g}{L_g L_f (C_f + C_g)}} + \omega_g) \\ p_{5,6} &= \pm j(\sqrt{\frac{L_f + L_g}{L_g L_f (C_f + C_g)}} - \omega_g) \end{cases} \tag{17}$$

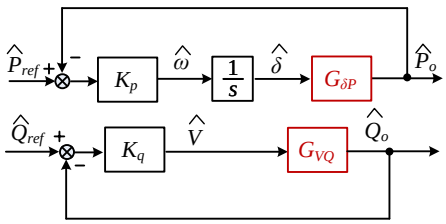


**Fig. 4:** Active and reactive power control block diagram of a GFM inverter.

For the condition that there is no ac capacitor, $G_{\delta P}$ and $G_{VQ}$ are reduced to the well-known forms given in previous works, e.g., in [3] and [12], i.e.

$$G_{\delta P} = \frac{a_0 s^2 + a_1 s + a_2}{(sL_g + R_g)^2 + (\omega_g L_g)^2} \tag{18}$$

$$G_{VQ} = \frac{b_0 s^2 + b_1 s + b_2}{(sL_g + R_g)^2 + (\omega_g L_g)^2} \tag{19}$$

where

$$\begin{aligned} a_0 &= \frac{L_g}{\omega_g}(v_g V_0 cos\delta_0 - V_0^2) \\ a_1 &= \frac{R_g}{\omega_g}(v_g V_0 cos\delta_0 - V_0^2) \\ a_2 &= \omega_g L_g v_g V_0 cos\delta_0 - R_g v_g V_0 sin\delta_0 \\ b_0 &= \frac{L_g}{\omega_g}(V_0 - v_g cos\delta_0) \\ b_1 &= \frac{R_g}{\omega_g}(V_0 - v_g cos\delta_0) \\ b_2 &= \omega_g L_g (2V_0 - v_g cos\delta_0) + R_g v_g sin\delta_0 \end{aligned} \tag{20}$$

It is clear that from (18) and (19) that only a pair of grid-fundamental-frequency resonant poles $p_{1,2} = \pm j\omega_g$ remain as ignoring $R_g$ under this condition.

However, the presence of the shunt ac capacitor introduces two additional pairs of complex poles ($p_{3,4}$ and $p_{5,6}$ in (17)), which contribute two additional resonant peaks in $T_P$, as shown in Fig. 5. It is known from (17) that the frequencies of $p_{3,4}$ and $p_{5,6}$ are dependent on the values of $L_g$, $L_f$ and $C_f$. Hence, when $C_g$ increases, the frequencies of $p_{3,4}$ and $p_{5,6}$ decrease, while the decreasing of $SCR$ can also lower the frequencies of $p_{3,4}$ and $p_{5,6}$, as shown in Fig. 5.

Moreover, if $\sqrt{\frac{L_f+L_g}{L_g L_f (C_f+C_g)}} < 2\omega_g$, the frequency of $p_{5,6}$ is lower than $\omega_g$ while the the frequency of $p_{3,4}$ is higher than $\omega_g$, as shown by the yellow solid line in Fig. 5 (a), otherwise both frequencies of $p_{3,4}$ and $p_{5,6}$ are higher than $\omega_g$, as shown by the blue dashed line in Fig. 5(a). These two different scenarios would have different impact on the controller design, which will be described in the Section.III.

## III. Active Damping Design

In order to guarantee the stable operation of the GFM inverter, the active damping resistor $k_v$ is usually adopted to

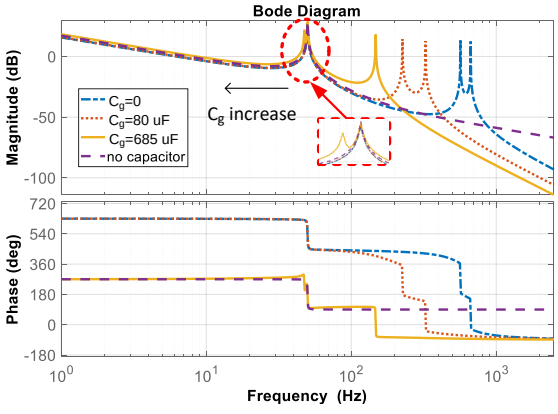


**(a)**

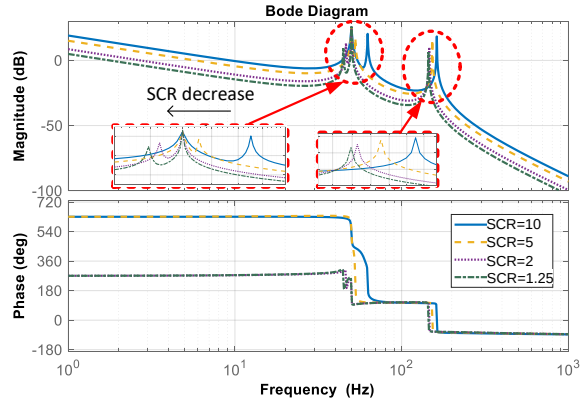


**(b)**

**Fig. 5:** Bode plot of $T_P$ without active damping. (a) $L_f = 5mH$, $L_g = 20mH$. (b) $L_f = 5mH$, $C_g = 685uF$.

dampen the resonant peaks in $T_P$. Moreover, $k_v$ is usually cascaded with a high-pass filter (HPF) $\frac{s}{s+\omega_v}$ to avoid its impact on the steady-state power control of the GFM inverter, as shown in Fig. 1, where $\omega_v$ represents the cutoff frequency of the HPF.

The selection of $\omega_v$ is critical since the active damping only remains effective in the frequency range higher than $\omega_v$ [6]. Hence, $\omega_v$ should be selected such that it is lower than the lowest frequency of resonant peaks in $T_P$. In previous works $\omega_v < \omega_g$ is suggested to dampen the grid-frequency resonant peak in $T_P$, which is the only resonant peak if there are no ac capacitors, as shown by the purple dotted line in Fig. 5 (a). Yet, this design guideline of $\omega_v$ should be re-investigated if there are shunt ac capacitors, due to the presence of two additional resonant peaks in $T_P$.

1. If $\sqrt{\frac{L_f+L_g}{L_g L_f (C_f+C_g)}} > 2\omega_g$, which corresponds to the case that GFM inverter is connected to a stiff grid (large $SCR$) and/or with small $C_g$. In this case, as shown in Fig. 5, the frequencies of the two additional resonant peaks introduced by the shunt ac capacitor are all larger than $\omega_v$. Hence, they can still be dampened by selecting $\omega_v < \omega_g$. As an example presented in Fig. 6 (a), where $L_f = 5mH$, $L_g = 20mH$,

**TABLE I:** Parameters used in the simulation and experiment

| | |
|---|---|
| Filter inductance $L_f$ | 5 mH |
| Filter capacitor $C_f$ | 20 uF |
| Shunt capacitor $C_g$ | 685 uF |
| Filter resistance $R_f$ | 0.01 Ω |
| Grid inductance $L_g$ | 20 mH |
| Grid resistance $R_g$ | 0.02 Ω |
| Grid voltage $V_g$ | 20 V |
| Active power control parameter $k_{pp}$ | 0.1 p.u. |
| Reactive power control parameter $k_{qp}$ | 0.03 p.u. |
| Grid frequency$\omega_g$ | 50 Hz |
| Switching frequency | 5000 Hz. |
| Rated active power $P_{ref}$ | 76 W |
| Active resistance $k_v$ | 0.05 p.u. |

$C_f = 20uF$ and $C_g$ is not present, the frequencies of two additional resonant peaks can be calculated as 612.98 Hz and 512.98 Hz. Since the frequencies of two additional resonant peaks are above $50Hz$, all resonant peaks in $T_P$ can be damped by selecting $\omega_v = 40Hz < \omega_g$, and the loop gain indicates the system is stable due to the positive phase margin (PM). In this scenario, the assumption in previous work that neglecting the impact of ac capacitors during the design of power control loops of GFM-VSC is justified [3].

2. If $\sqrt{\frac{L_f+L_g}{L_gL_f(C_f+C_g)}} < 2\omega_g$, which corresponds to the case that GFM inverter is connected to a weak grid (small $SCR$) and/or with large $C_g$ (introduced by the local capacitive load or shunt capacitor used for reactive power compensation). In this case, it is known from (17) that the frequency of the complex poles $p_{5,6}$ (which is defined as $\omega_{res1}$ hereafter) is lower than $\omega_g$, which can only be effectively damped by selecting $\omega_v < \omega_{res1}$, rather than $\omega_v < \omega_g$. In this scenario, the impact of ac capacitors cannot be neglected when designing power control loops of GFM-VSC, otherwise the resonant peak at $\omega_{res1}$ cannot be identified and there is a risking in selecting $\omega_v$ in the range between $\omega_{res1}$ and $\omega_g$ that could destabilize the system. This is demonstrated by an example given in Fig. 6 (b). With parameters given in Table I, it can be calculated that $\omega_{res1} = 44.77Hz$. By selecting $\omega_v = 45Hz < \omega_g$, the resonant peak at $\omega_{res1}$ cannot be damped and the system is unstable because of the negative phase margin of the loop gain, as the blue solid line shown in Fig. 6 (b). In contrast, the system can be stabilized by selecting $\omega_v = 20Hz < \omega_{res1} = 44.77Hz$, as the red dotted line shown in Fig. 6 (b). Nevertheless, by neglecting the impact of ac capacitor, both $\omega_v = 20Hz$ and $\omega_v = 45Hz$ yield a stable loop gain, as shown in Fig. 6 (a), which leads to a misleading stability prediction.

## IV. Simulation and Experiment

### A. Simulation Results

To verify the theoretical analysis, the time-domain simulations are carried out in MATLAB/Simulink and PLECS blockset with detailed electronic model presented in Fig. 1. The main parameters given in Table I are adopted.

Fig. 7 shows the simulation results of the active power with $\omega_v$ changing from $20Hz$ to $45Hz$ at 1.7s. As the $C_g$ is connected at the PCC, the system cannot be stable after the increasing of $\omega_v$, resulting in a 44.7Hz oscillation in the active power, as shown in Fig. 7(b), which verifies the stability prediction in Fig. 6(b). However, the system can still be stable with $\omega_v = 45Hz$ if there is no $C_g$, as shown in Fig. 7(a), and is in accordance with the theoretical analysis given in Fig. 6 (a).

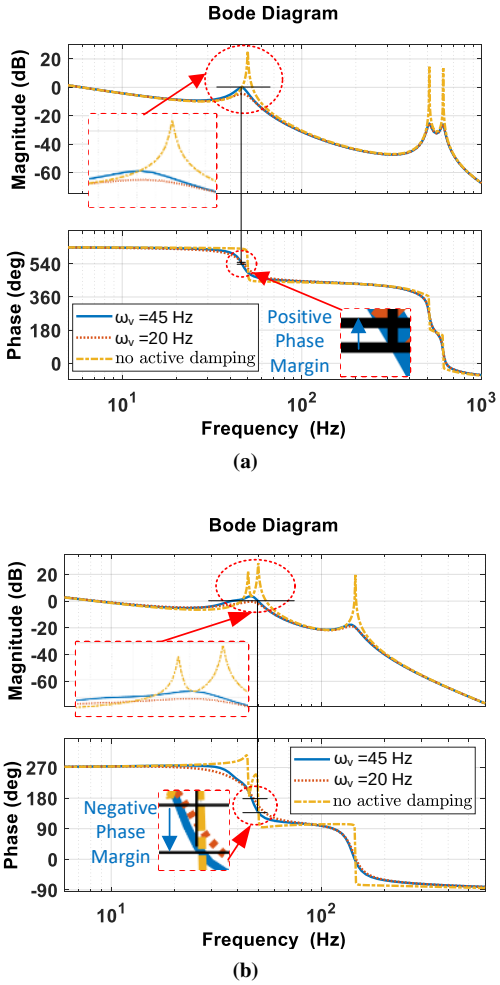


**Fig. 6:** Bode diagram of $T_P$ with active damping and different $\omega_v$. (a) Without $C_g$. (b) With $C_g$.

### B. Experimental Results

To further verify the simulation results, the experiments are carried out with a three-phase grid-connected inverter. The parameters used in the experiments are the same with the ones used in the simulation.

Fig. 8 shows that the experimental results are consistent with the simulation results. The system that contains $C_g$ becomes unstable after $\omega_v$ changes from $20Hz$ to $45Hz$, as shown in Fig. 8 (b), while it can still maintain stable without $C_g$, as shown in Fig. 8 (a). The experimental results are in well accordance with the simulation results and thus the accuracy of the theoretical analysis is verified.

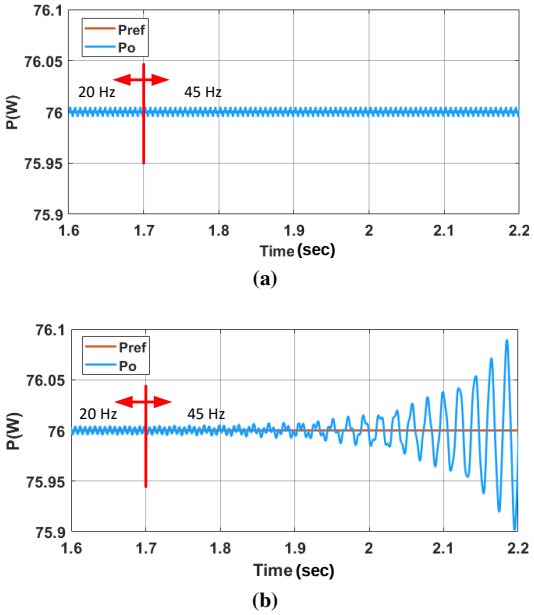


**Fig. 7:** Simulation results for active power. (a) Without $C_g$. (b) With $C_g$.

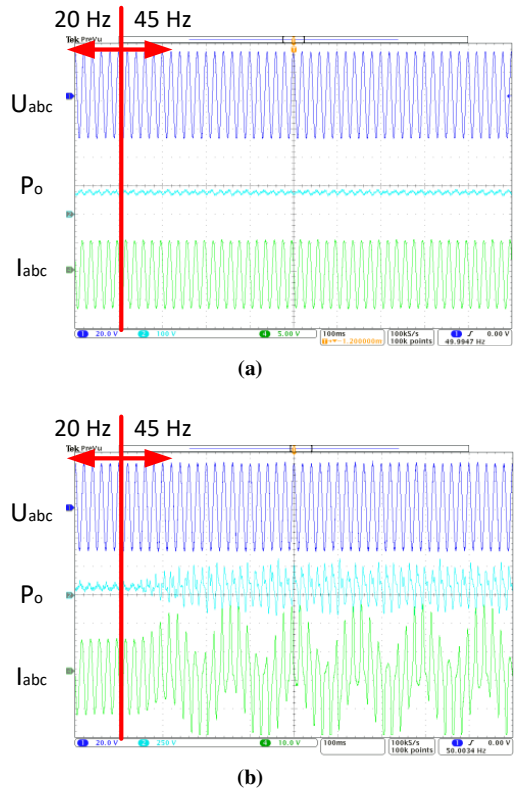


**Fig. 8:** Experimental results for active power. (a) Without $C_g$. (b) With $C_g$.

## V. Conclusion

This paper demonstrates that the presence of shunt ac capacitors introduces two additional resonant peaks in the loop gain of power control loops. The lowest frequency of these resonant peaks becomes $\omega_{res1} = \sqrt{\frac{L_f+L_g}{L_g L_f (C_f+C_g)}} - \omega_g$. Therefore, to stabilize the GFM inverter, the cutoff frequency of HPF used in the active damping control should be selected with the value of $\omega_{res1}$ considered. Simulation and experimental tests are carried out to corroborate the theoretical analysis.

## References


[1] J. Matevosyan, B. Badrzadeh, T. Prevost, E. Quitmann, D. Ramasubramanian, H. Urdal, S. Achilles, J. MacDowell, S. H. Huang, V. Vital, J. O'Sullivan, and R. Quint, "Grid-forming inverters: Are they the key for high renewable penetration?" *IEEE Power and Energy Magazine*, vol. 17, no. 6, pp. 89–98, 2019.

[2] H. Wu and X. Wang, "Virtual-flux-based passivation of current control for grid-connected vscs," *IEEE Transactions on Power Electronics*, vol. 35, no. 12, pp. 12 673–12 677, 2020.

[3] L. Zhang, L. Harnefors, and H.-P. Nee, "Power-synchronization control of grid-connected voltage-source converters," *IEEE Transactions on Power Systems*, vol. 25, no. 2, pp. 809–820, 2010.

[4] L. Zhang, L. Harnefors, and N. Johansson, "Power-system modeling - a transfer matrix approach," in *11th IET International Conference on AC and DC Power Transmission*, 2015, pp. 1–8.

[5] S. I. Nanou and S. A. Papathanassiou, "Grid code compatibility of vsc-hvdc connected offshore wind turbines employing power synchronization control," *IEEE Transactions on Power Systems*, vol. 31, no. 6, pp. 5042–5050, 2016.

[6] L. Harnefors, M. Hinkkanen, U. Riaz, F. M. M. Rahman, and L. Zhang, "Robust analytic design of power-synchronization control," *IEEE Transactions on Industrial Electronics*, vol. 66, no. 8, pp. 5810–5819, 2019.

[7] L. Zhang, L. Harnefors, and H.-P. Nee, "Modelling and control of vsc-hvdc connected to island systems," in *IEEE PES General Meeting*, 2010, pp. 1–8.

[8] J. Rocabert, A. Luna, F. Blaabjerg, and P. Rodríguez, "Control of power converters in ac microgrids," *IEEE Transactions on Power Electronics*, vol. 27, no. 11, pp. 4734–4749, 2012.

[9] H. Wu, X. Ruan, D. Yang, X. Chen, W. Zhao, Z. Lv, and Q.-C. Zhong, "Small-signal modeling and parameters design for virtual synchronous generators," *IEEE Transactions on Industrial Electronics*, vol. 63, no. 7, pp. 4292–4303, 2016.

[10] T. Messo, J. Jokipii, J. Puukko, and T. Suntio, "Determining the value of dc-link capacitance to ensure stable operation of a three-phase photovoltaic inverter," *IEEE Transactions on Power Electronics*, vol. 29, no. 2, pp. 665–673, 2014.

[11] T. Suntio, T. Messo, and J. Puukko, *Power electronic converters: dynamics and control in conventional and renewable energy applications*. John Wiley & Sons, 2017.

[12] D. Pan, X. Wang, F. Liu, and R. Shi, "Transient stability of voltage-source converters with grid-forming control: A design-oriented study," *IEEE Journal of Emerging and Selected Topics in Power Electronics*, vol. 8, no. 2, pp. 1019–1033, 2020.